Atmospheric
Chemistry
and Physics

Estimating regional-scale methane flux and budgets using CARVE aircraft measurements over Alaska

Sean Hartery[1], Róisín Commane[2], Jakob Lindaas[2], Colm Sweeney[3,4], John Henderson[5], Marikate Mountain[5], Nicholas Steiner[6], Kyle McDonald[6], Steven J. Dinardo[7], Charles E. Miller[7], Steven C. Wofsy[2], and Rachel Y.-W. Chang[1,2]

[1]Department of Physics and Atmospheric Science, Dalhousie University, Halifax NS, USA
[2]School of Engineering and Applied Sciences, Harvard University, Cambridge MA, USA
[3]Global Monitoring Division, National Oceanic and Atmospheric Administration Earth System Research Laboratory, Boulder CO, USA
[4]Cooperative Institute for Research in Environmental Sciences, University of Colorado, Boulder CO, USA
[5]Atmospheric and Environmental Research, Inc., Lexington MA, USA
[6]Department of Earth and Atmospheric Science, City College University of New York, New York NY, USA
[7]Jet Propulsion Laboratory, California Institute of Technology, Pasadena CA, USA

Correspondence: Rachel Y.-W. Chang (rachel.chang@dal.ca)

Abstract. Methane (CH_4) is the second most important greenhouse gas but its emissions from northern regions are still poorly constrained. In this study, we analyze a subset of in situ CH_4 aircraft observations made over Alaska during the growing seasons of 2012–2014 as part of the Carbon in Arctic Reservoirs Vulnerability Experiment (CARVE). Net surface CH_4 fluxes are estimated using a Lagrangian particle dispersion model which quantitatively links surface emissions from Alaska and the western Yukon with observations of enhanced CH_4 in the mixed layer. We estimate that between May and September, net CH_4 emissions from the region of interest were 2.2 ± 0.5 Tg, 1.9 ± 0.4 Tg, and 2.3 ± 0.6 Tg of CH_4 for 2012, 2013, and 2014, respectively. If emissions are only attributed to two biogenic eco-regions within our domain, then tundra regions were the predominant source, accounting for over half of the overall budget despite only representing 18 % of the total surface area. Boreal regions, which cover a large part of the study region, accounted for the remainder of the emissions. Simple multiple linear regression analysis revealed that, overall, CH_4 fluxes were largely driven by soil temperature and elevation. In regions specifically dominated by wetlands, soil temperature and moisture at 10 cm depth were important explanatory variables while in regions that were not wetlands, soil temperature and moisture at 40 cm depth were more important, suggesting deeper methanogenesis in drier soils. Although similar environmental drivers have been found in the past to control CH_4 emissions at local scales, this study shows that they can be used to generate a statistical model to estimate the regional-scale net CH_4 budget.

1 Introduction

Recent trends in observed global atmospheric methane (CH_4) mole fractions have shown increases since a short-lived stabilization period in the early 2000s and have increased by ~ 150 % from pre-industrial values (Dlugokencky et al., 2011; Kirschke et al., 2013; Ciais et al., 2014). As the second most potent anthropogenically emitted greenhouse gas after carbon dioxide (CO_2) in terms of total radiative forcing, CH_4 can account for 20 % of recent trends in global surface air temperatures, which have risen by approximately 0.6 K over the past century (Kirschke et al., 2013; Ciais et al., 2014). Since emissions of CH_4 from wetlands represent ~ 30 % of the global CH_4 produced annually, it is of critical scientific interest to determine whether these sources will strengthen in a warming climate (Whalen, 2005; Kirschke et al., 2013; Ciais et al., 2014). It has been speculated that increased air temperatures in wetlands north of 40° N, combined with ecological, hydrological, and biogeochemical changes, could couple into a temperature–emissions feedback, whereby or-

ganic carbon previously sequestered in below-ground permafrost thaws is subsequently metabolized into atmospheric CH$_4$ by local methanogen communities (Schuur et al., 2015; Tarnocai et al., 2009).

Temperatures have increased dramatically in Arctic regions, which have seen almost 3 K increases in air temperatures since the beginning of the 20th Century (Overland et al., 2015), with 1.8 K occurring over the past 3 decades (Collins et al., 2013). Rising surface air temperatures have resulted in a response in soil temperatures, with winter-time observations of permafrost core temperatures in Alaska showing increases of approximately 3–4 K on the Arctic Coastal Plain of Alaska at borehole depths of 5–20 m and 1–2 K in the Brooks Range at depths of 20 m (Osterkamp, 2005). If current Arctic climate trends continue, up to 10–30 % of permafrost in Arctic lowlands could significantly degrade, leading to measurable ecological shifts and adding new labile organic carbon to the carbon cycle (Jorgenson et al., 2006).

From a biogeochemical perspective, CH$_4$ is produced in soils below the water table, which provide the anaerobic conditions necessary for fermentation of soil organic carbon stocks (Whalen, 2005). The fermented organic carbon products are then consumed by methanogenic archaea within the soil column, producing CH$_4$ gas (Whalen, 2005). As CH$_4$ production is a biological process relying on microbial activity, it is commonly observed that high CH$_4$ emissions are coincident with warm wetland soils (Sturtevant et al., 2012; Olefeldt et al., 2013; Kirschke et al., 2013; Christensen, 1993).

In Alaska and the neighbouring Yukon, seasonal wetlands make up nearly 12 % of the total surface area (Bergamaschi et al., 2007), with 92 % of soils within continuous permafrost zone (Hugelius et al., 2013). Since this region is frozen most of the year, its carbon stocks have long been preserved within permafrost, limiting carbon mobilization through respiration. In spite of recent warming and mobilization of sequestered carbon, a recent study of atmospheric mole fractions of CH$_4$ in the North Slope of Alaska found no significant increase in annual CH$_4$ emissions over the past 29 years (Sweeney et al., 2016). Field observations have also reported that microbial communities linked to CH$_4$ oxidation thrive in soils with low moisture content (Xue et al., 2016), highlighting that a warming climate may not have a one-to-one effect on biogenic CH$_4$ flux at a regional scale.

Numerous past studies have been conducted in permafrost regions such as Alaska at the scale of chambers (as summarized by Olefeldt et al., 2013) and eddy-covariance towers (e.g. Fan et al., 1992; Sturtevant et al., 2012; Zona et al., 2016), providing insight into factors controlling CH$_4$ emissions at the scale of ~ 1 m to ~ 1 km. These studies have revealed that CH$_4$ emissions are spatially inhomogeneous at those scales and are highly dependent on local conditions such as soil moisture, temperature, elevation, and soil carbon. While these process-based studies are extremely important, extrapolating the results to larger scales can be chal-

lenging, although not impossible (e.g. O'Shea et al., 2014). At the other extreme, top-down inversion studies estimate global CH$_4$ emissions using measurements from surface sites around the world and/or satellite observations coupled to sophisticated transport models (Bruhwiler et al., 2014; Bergamaschi et al., 2013; Chen and Prinn, 2006). These results provide insight into regional emissions; however, it is more difficult to understand local drivers that affect emission rates. More recently, tall towers, either alone or in a network, and aircraft observations have been used to study regional emissions of CH$_4$ from permafrost areas (Karion et al., 2016; Sasakawa et al., 2010; Chang et al., 2014). Tall towers are advantageous since their operation is less dependent on weather conditions than static chamber measurements, they provide continuous measurements, and their footprint spans a much larger area than a typical eddy-covariance tower. Despite this, in a region like Alaska, where high mountains significantly affect transport patterns, a single tower may not be sensitive to the entire region throughout the year (Karion et al., 2016). In contrast, aircraft observations, by virtue of their mobile platform, can sample larger regions and can periodically measure in the free troposphere to establish background levels. However, their coverage is dependent on weather conditions.

In this study, we estimate net surface CH$_4$ fluxes using in situ observations of CH$_4$ from an aircraft that flew in Alaska as part of the Carbon in Arctic Reservoirs Vulnerability Experiment (CARVE). This work uses similar methods to those used by Chang et al. (2014), but extends the analysis to include the growing seasons of 2013 and 2014 and explores how their inter-annual and intra-annual variability can be explained by hydrological and environmental controls at a regional scale. A recent study by Miller et al. (2016) explores similar questions using a more complex geostatistical inversion model constrained by a much larger data set. Using multiple linear regression models, we investigate the relationship between land surface properties and observed atmospheric CH$_4$. Our method finds similar results to the complex geostatistical inversion model employed by Miller et al. (2016) and could provide a simple diagnostic tool for regional methane cycle analysis.

2 Methods

2.1 Description of aircraft flights

The data presented in this study were collected on board a National Aeronautics and Space Agency (NASA) C23-B aircraft during the Alaskan growing seasons of 2012–2014. In 2012, flights occurred in the last 2 weeks of each month from May to September for a total of 31 flight days and 212 flight hours. In 2013 and 2014, flights occurred in the first 2 weeks of each month from April to October and May to November, resulting in 290 and 300 flight hours over 42 and 48

flight days, respectively. All flights analyzed in this study originated from Fairbanks, AK, and stayed within Alaska. Not all regions and altitudes were sampled every month since the flight routes were limited by icing concerns and weather conditions. Data were typically acquired at 150 m above ground level (a.g.l.) to maximize sensitivity to local surface–atmosphere fluxes; however, periodic profiling of the atmosphere to 5–6 km a.g.l. occurred throughout the flights to characterize planetary boundary layer height and mole fractions in the free troposphere.

2.2 Measurements

Mole fractions of CH$_4$, CO$_2$, carbon monoxide (CO), and water vapour (H$_2$O) were measured in situ every $\sim$2.5 s using two independent cavity ring-down spectrometers. Each system had an individual rear-facing inlet on the port side of the aircraft. Sample flow from the inlets passed through a length of Synflex tubing with an approximate transit time of 30 ± 2 s. The first system (Picarro; G1301-m in 2012, G2401-m in 2013 and 2014) directly sampled the air without any pre-treatment and alternately sampled from one of two on-board calibration cylinders every 30 min. These onboard calibration cylinders were changed throughout the campaigns as the pressure approached 3.4 MPa (500 psi). They were calibrated by NOAA before and after each deployment. Calibration for the water vapour correction was conducted on the flight instrument before and after each year's campaign according to Chen et al. (2010). Further details of this system can be found in Karion et al. (2013).

The sample flow in the second system first passed through a 0.2 μm Teflon filter before passing through a Nafion dryer followed by a dry ice trap which effectively lowered the dewpoint temperature of the sample flow to $\sim$195 K before entering the spectrometer (Picarro; G2401-m). This reduced the water vapour of the sample flow to < 0.001 % and allowed dry mole fractions of CH$_4$, CO$_2$, and CO to be directly measured. Two onboard 8 L calibration cylinders (independent of the first system's) were sampled at the beginning and end of every flight as well as every 30 min during flight. These in-flight calibrations were linearly interpolated between calibration times to generate time-varying calibration curves. In-flight calibrations that were greater than 2.5 standard deviations away from the mean of the calibrations for a given flight were excluded.

Before each year's campaign, the onboard calibration cylinders for the second system were flushed twice and then filled from 30 L fill tanks (Scott Marrin, Inc., Riverside, CA). Due to the longer sampling seasons in 2013 and 2014, the onboard calibration tanks were topped up once in each of those years with the original fill tanks before the pressure dropped below 3.4 MPa. Both the original fill tanks from Scott Marrin and the onboard calibration cylinders were calibrated in the laboratory with the spectrometer used in-flight before and after each year's campaign using tanks with known mole fractions obtained from NOAA, tying our measurements to the WMO scales (Dlugokencky et al., 2005; Novelli et al., 1994; Zhao and Tans, 2006). The differences in mole fractions before and after each year's flight campaigns in both the onboard calibration cylinder and the fill tanks were less than 0.15 ppm for CO$_2$, 0.8 ppb for CH$_4$ and 7 ppb for CO, all of which were within the precision of the system. The mole fraction in the on-board calibration cylinders was therefore treated as constant throughout each year's study and assumed to be unaffected by the addition of gas. It was also assumed that any changes within any of the tanks were negligible throughout each year's campaign.

The one deviation was that the onboard calibration cylinders were not calibrated before the 2012 deployment due to time constraints. However, these cylinders were calibrated after the 2012 campaign and compared to the fill tanks calibrated before and after that year's campaign. Except for CO$_2$ in one of the onboard calibration cylinders, which was 0.29 ppm lower than the fill tank, the comparison with the fill tanks for the other gases all fell into the ranges given above. In the case of this exception, the post-mission calibration of the onboard calibration cylinder was used since the tank was not topped up during that year's mission.

Comparison of the two systems showed a mean difference of 0.8, 0.3, and 0.4 ppb for CH$_4$ for 2012, 2013, and 2014, respectively, with no dependence on water vapour levels ($r^2 = 0.008$). The mole fractions presented in this study merges those measured by both systems, to fill in times when one of the systems was calibrating or functioning imperfectly. The system used to gap-fill is offset by the mean difference between the two systems for a given flight. Since our analysis is based on the difference between mole fractions in the free troposphere and the mixed layer (see below), this treatment does not bias our analysis. The greenhouse gas measurements were merged to a common 5 s timescale along with the location data, measured using a global positioning unit (GPS) (Crossbow; NAV420); outside air pressure (Parascientific; 745-15A); outside air temperature (Harco; 100366-18), dew-point temperature (Edgetech; Vigilant); and ozone (2B Technologies; 205).
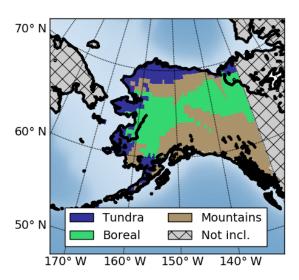
3 Analysis methods

3.1 Footprint sensitivity

To identify the contribution by upwind surface processes to observed mole fractions of CH$_4$, source–receptor relationships ("footprints"), that represent the adjoint of the transport model, were computed using a Lagrangian particle dispersion model (LPDM) driven by three-dimensional winds from a regional high-resolution numerical weather prediction model. Specifically, the Weather Research and Forecasting (WRF; Skamarock et al., 2008) regional numerical weather prediction model was coupled offline to the Stochas-

tic Time-Inverted Lagrangian Transport Model (STILT; Lin et al., 2003). The coupling of the STILT model with WRF meteorological fields, hereafter WRF–STILT, is described by (Nehrkorn et al., 2010). The polar variant of WRF (Hines et al., 2011; Bromwich et al., 2009; Hines and Bromwich, 2008) coupled with STILT was configured for the Arctic CARVE domain by (Henderson et al., 2015), who provide a detailed description and meteorological validation of the high-resolution simulations performed on a 3.3 km grid suitable for simulating particle transport on regional scales in mountainous terrain. Their initial STILT footprints from WRF v3.4.1 were used in the analysis of (Chang et al., 2014). The current investigation uses WRF v3.5.1 and incorporates recently available PIOMAS cryosphere fields (Zhang and Rothrock, 2003; Hines et al., 2015) and footprints on an expanded circumpolar domain north of 30° N.

To avoid unnecessary computational costs, measurement locations that occurred below 1 km a.g.l. were placed into discrete bins on a grid of 5 km in the horizontal and 50 m in the vertical, while locations above 1 km a.g.l. were similarly binned 5 km in the horizontal and 100 m in the vertical (Chang et al., 2014; Commane et al., 2017). These spatial bins were then used as receptor points for each STILT simulation. Measurement times were also truncated to the hour to match the time resolution of the meteorological fields. The use of WRF at high resolution to drive the STILT model results in higher-fidelity meteorological fields and subsequent transport calculations than afforded by most global reanalysis (Nehrkorn et al., 2010; Henderson et al., 2015).

To derive source–receptor relationships, each STILT simulation launched 500 particles into the atmosphere at the location of each receptor point and traced their dispersion through the atmosphere in reverse time over 10 days via three-dimensional advective winds and stochastic (i.e. random, probabilistic) processes determined from the underlying meteorology (Lin et al., 2003; Henderson et al., 2015). Every hour, particles that were in the lower half of the boundary layer were assumed to be influenced by the surface (Gerbig et al., 2003, see the Supplement for further discussion about this assumption) and are gridded to generate a footprint sensitivity plot for that hour. The footprint used in this analysis was calculated on a $0.5° \times 0.5°$ latitude–longitude grid, with a unit of abundance flux^{-1} (e.g. ppb (nmol m^{-2} s^{-1})$^{-1}$, where ppb is parts per billion) (Lin et al., 2003), and allows us to relate upwind surface influence to an observation at a given time and location. These footprints are therefore species-independent. The original STILT runs simulated transport 10 days backward in time (Henderson et al., 2015). However, as discussed in the next section, our analysis only uses the first 5 days. Past studies that have used WRF–STILT footprint sensitivities for this region have been successful in attributing fluxes of CO_2 (Commane et al., 2017; Karion et al., 2016), a much harder problem due to its bi-directional flux and strong diurnal cycle. These studies were therefore much more reliant on WRF–STILT generating accurate foot-
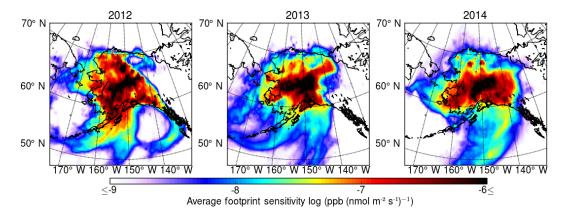

Figure 1. Eco-regions derived from the Commission for Environmental Cooperation Level II Terrestrial Eco-regions. The study region is defined by the coastline and filled eco-regions.

prints during both day and night compared to our study. The success of these past CO_2 studies gives us confidence in the footprint sensitivities used in this analysis.

3.2　Domain

This analysis focuses on the influence of surface emissions from Alaska and Yukon on observed CH_4 mole fractions. To this end, we restricted our region of interest to 50–75° N and 130–170° W (Fig. 1) and only consider footprint sensitivity derived from WRF–STILT during the first 5 days preceding each receptor point. The timescale of 5 days was chosen because sources outside the domain are expected to have transport timescales roughly equal to that of free-tropospheric mixing and therefore only contribute to background values of CH_4. Figure 2 shows the cumulative 5-day footprint of our analyzed times for each year averaged over the number of profiles in each year and shows that our observations are mostly influenced by the boreal interior of Alaska as well as tundra regions. It should be noted that although our mean footprints were more sensitive in the North Slope of Alaska in 2012, our absolute sensitivity was comparable in all 3 years due to the increased number of flights in 2013 and 2014.

Our choice of the spatial domain was determined by the distribution of 5-day footprints. As will be defined in the subsequent section concerning the mixed layer, footprint sensitivity simulations that had less than 1.0 ppb (nmol m^{-2} s^{-1})$^{-1}$ total land sensitivity were identified as being in the free troposphere, following Henderson et al. (2015). For an idealized homogeneous distribution of sensitivity, where an air parcel is equally sensitive to all land areas within the domain, this threshold would translate to $\sim 1 \times 10^{-4}$ ppb (nmol m^{-2} s^{-1})$^{-1}$ in any given grid

Figure 2. The average footprint sensitivity calculated from WRF–STILT is shown for all receptor points modelled within the profiles included in the analysis (2012–2014).

cell. It was assumed that areas of the globe with sensitivities smaller than this threshold did not significantly contribute to CH$_4$ enhancements, since, even at extreme fluxes of 1000 mg m^{-2} d^{-1}, they would contribute < 0.1 ppb to the observed enhancement. In the cumulative 5-day footprints shown in Fig. 2, 71 % of the footprint that exceeded the grid-cell threshold was from land in the chosen domain, while 29 % could be sourced to oceans. It is worth noting that the previous study of Chang et al. (2014) restricted its domain to 135° W. While the May–September footprints showed that < 2 % of the footprint originated in regions east of 135° W, it was found that at least 5 % of the total land sensitivity in April, October, and November came from the Canadian Yukon. Of all the land surface influence on our observations, only 0.3 % originated from land outside of our study region, suggesting that our sampling strategy and choice of domain allowed our observations to be most sensitive to surface emissions from the study region.

3.3 Mixed layer

We use the term "mixed layer" to refer to the combination of both the residual layer and the boundary layer throughout the remainder of this paper. As our footprints predict the sensitivity to surface influences 5 days prior to a measurement, both local and regional sources need to be considered. As a general approximation, CH$_4$ enhancements in the boundary and residual layers reflect local and regional surface emissions, while the portion of a vertical profile above the mixed layer can be used to represent background levels. In practice, the footprint sensitivity maps attribute the spatial distribution of sources that influence a particular receptor, whether it is in the boundary layer or residual layer. It should be noted that particles in the residual layer do not contribute to the footprint at that specific time but carry surface influence from earlier time spent in the boundary layer and therefore may have elevated surface influence compared to background values.
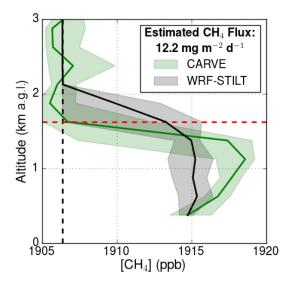
We estimate the bottom of the free troposphere (h) by calculating the refractivity (N) using parameters measured at different altitudes on the aircraft (Chan and Wood, 2013; Bean and Dutton, 1966):

$$N = 77.6 \frac{P}{T} + 3.77 \times 10^5 \frac{P_{\mathrm{w}}}{T^2}, \tag{1}$$

where P and P_{w} (hPa) are the atmospheric pressure of air and water, respectively, and T (K) is the atmospheric temperature. The height at the minimum of the gradient in N is the top of the mixed layer.

Tables S1–S3 in the Supplement list every time the aircraft flew between 200 m and at least 2.7 km as an individual profile. In analyzing these profiles, it was often found that this method overestimated the mixed layer height compared to profiles of CH$_4$, O$_3$, and the total land surface sensitivity calculated by WRF–STILT; as a secondary calculation, the height at which WRF–STILT sensitivities dropped below 1.0 ppb (nmol m^{-2} s^{-1})$^{-1}$ was used to approximate h (Henderson et al., 2015). Upon individual inspection of profiles, it was found that in 25 % of cases (i.e. 68 profiles) neither method captured an h which correctly separated the free troposphere and mixed layer. After removing these profiles, a further 25 % of profiles within the remaining set (i.e. 50) had h differing by > 750 m between the two methods (paired t test; $p < 0.005$). In these cases, either the boundary layer dynamics within WRF–STILT were not representative of local meteorology or there was too much variance about the minimum of the gradient in N. Therefore, these profiles were not included in the analysis. In the final set of profiles used for analysis, a paired t test found that the two methods did not statistically differ from each other ($p > 0.1$) and both agreed to within 500 m ~ 90 % ($r^2 = 0.6$) of the time. We attempted to use other variables such as virtual potential temperature to define the mixed layer but the methods described above gave the most consistent results.

Across all years, h was found to occur between 1.1 and 1.8 km with a median of 1.5 km above Alaska, consistent

Figure 3. A sample profile from 3 September 2014 at 65° N, 148.6° W. Shaded regions denote the minimum and maximum of the ranges and the solid line is the median. The dashed red line represents h, and the dashed black line is [CH$_4$]$_0$.

with estimates derived from satellite retrievals (Chan and Wood, 2013). On average, h in May–September was 30 % higher than in April, October, or November. These findings are consistent with lower solar zenith angles and shorter solar days in colder months, both of which reduce the strength of convective forces which form the boundary layer (Stull, 1988).

3.4 CH$_4$ flux estimates

In this analysis, we use column enhancements of CH$_4$ (ΔCH$_4$) to estimate net surface fluxes (Commane et al., 2017; Chang et al., 2014; Gatti et al., 2014; Chou et al., 2002). This method assumes that CH$_4$ enhancements below h that are above background levels are a result of interactions with the local surface that are not well mixed with the free troposphere. Net surface fluxes are determined by calculating the corresponding surface influence at each height in the column using the footprint sensitivities determined from WRF–STILT. This method of calculating ΔCH$_4$ is less reliant on the accurate simulation of the vertical structure of the atmosphere as well as turbulent transport in the lower atmosphere. Instead, we rely on the integrated model simulation to match the integrated observations. The majority of the measurements from the aircraft flights were in the surface layer. As such, this method also reduces bias in regional emission estimates by focussing on measurements throughout the atmosphere.

To calculate ΔCH$_4$, measurements in a vertical profile were first block-averaged by altitude into 250 m bins. A sample of such a profile observed during the CARVE campaign is shown in Fig. 3 and shows median, minimum, and maximum

[CH$_4$] observed in each 250 m bin up to 3 km along with the estimated CH$_4$ flux from the WRF–STILT footprint influence according to Eq. 3. In this sample profile, the calculation of the refractive index (N) properly captured the transition from the mixed layer to the free troposphere and WRF–STILT adequately modelled the mixed layer, leading to a reasonable estimate of CH$_4$ flux. Using h as the upper bound on the section of the profile affected by local sources and sinks,

$$\Delta CH_4 = \int_0^h ([CH_4](z) - [CH_4]_0) \frac{P_d(z)}{R^* T(z)} dz, \qquad (2)$$

where ΔCH$_4$ (nmol CH$_4$ m^{-2}) is the column integrated mixed layer enhancement of CH$_4$, [CH$_4$]$_0$ is the background CH$_4$ estimated by averaging the lowest 1 km in the free troposphere, P_d is the calculated atmospheric pressure of dry air using measurements of P and P_w, R^* is the universal gas constant, and z is the height a.g.l. as calculated from the height above sea level measured by the GPS and an underlying digital elevation map within the input meteorology of WRF. As an entrainment zone between the free troposphere and mixed layer was usually evident in profiles of CH$_4$, 500 m was added to h for our estimate of [CH$_4$]$_0$. Since [CH$_4$]$_0$ is typically stable with altitude in the free troposphere, this should not affect the integral in Eq. (2).

A similar calculation was undertaken for the corresponding footprint sensitivity, with the cumulative 5-day footprint at each height replacing ([CH$_4$](z) − [CH$_4$]$_0$) in Eq. (2), to calculate the sensitivity of the entire mixed layer to the surface (ΔI with units of nmol CH$_4$ m^{-2} (nmol m^{-2} s^{-1})$^{-1}$). As a first estimate, our a priori CH$_4$ flux is assumed to be uniformly emitting from our entire domain. Surface contributions outside of the study domain were excluded, as were seas and mountains, which we assume to be neither sources nor sinks of atmospheric CH$_4$ and therefore to not contribute to ΔCH$_4$. The total mixed layer sensitivity, ΔI, is then scaled to match ΔCH$_4$ to estimate CH$_4$ flux, $\hat{E}$:

$$\hat{E} = \frac{\Delta CH_4}{\Delta I}, \qquad (3)$$

with appropriate unit conversion to mg CH$_4$ m^{-2} d^{-1}. The estimation of uncertainties in CH$_4$ flux using Eq. (3) will be discussed in Sect. 3.7.

Monthly-mean CH$_4$ flux ($\overline{E}$) was estimated by weighting individual flux estimates by the total footprint sensitivity of each profile (Chang et al., 2014; Karion et al., 2016), so that

$$\overline{E} = \frac{(\sum \hat{E} \times \Delta I)}{\sum \Delta I} = \frac{\sum \Delta CH_4}{\sum \Delta I}. \qquad (4)$$

This biased the average towards profiles with larger spatial coverage and helped normalize profiles with lower ΔI, which sometimes resulted in high estimates of $\hat{E}$. The residuals of individual estimates against these monthly means are

shown in Fig. S2 of the Supplement. Their normal distribution about the trend in the monthly mean suggests that this method of weighted averaging was successful in mitigating biases in CH$_4$ flux stemming from differences in footprint sensitivity.

Growing-season budgets were calculated by integrating the monthly emissions from May through September and over our study domain (excluding mountains). The surface area of our domain was estimated using a digital elevation map from the Advanced Spaceborne Thermal Emission and Reflection Radiometer (ASTER) to estimate the enhancement of surface area in sloped terrain (Jenness, 2004). A land–ocean mask at $0.1° \times 0.1°$ was then used to approximate the fraction of land cover at $0.5° \times 0.5°$ to estimate surface area in coastal grid cells (i.e. $A_{land} = A^* f_{land}$). The total land surface area of our domain is estimated to be 2.1 million km^2 including mountains and 1.04 million km^2 without.

Since the goal of this study is to understand biogenic CH$_4$ emissions, observations influenced by combustion were excluded. Measurements of CO were used as an atmospheric tracer for air influenced by biomass burning events or oil development off-gassing, which co-emit CO and CH$_4$. Any profile which had measurements of CO exceeding 150 ppb within the mixed layer was not used in the analysis. This threshold was determined by observing that the annual distribution of CO deviates from normal above 150 ppb (Chang et al., 2014). It should be noted that our calculations only estimate net CH$_4$ emissions from non-mountainous land surfaces. These estimates include all processes such as biogenic, thermogenic, and non-combustion-related anthropogenic sources and sinks. We assume that the latter two processes are small compared to biogenic sources over the study domain; however, were this not true, our values could still be considered upper estimates for net biogenic emissions.

After CO screening, each individual vertical profile was assessed on a case-by-case basis to ensure that the WRF–STILT model adequately captured a mixed layer (i.e. the footprint sensitivity attenuated to zero as altitude increased) and that the estimated h from WRF–STILT clearly separated the mixed layer from the free troposphere. Of the 273 profiles identified, 9 were rejected due to excessive CO mole fractions. In addition, 118 were rejected using the two methods described in Sect. 3.3. The remaining 146 profiles, just under half of all the profiles, were kept for analysis. While this is a severe reduction in data, footprint sensitivity plots comparing the total footprint sensitivity of all the receptor points within all profiles against the total footprint sensitivity of those within the profiles kept for analysis showed no significant bias. As a result, this subset is thought to be both representative of the CARVE sampling campaign and free from errors in integration limits.

3.5 Eco-region dynamics

The previous assumption that the study region emits CH$_4$ uniformly is correct only to the zeroth order. It serves as the best estimate for the total magnitude of net flux and provides the most robust regional budget calculations. However, this assumption misses much of the spatiotemporal heterogeneity observed in emissions across and even within different biological and hydrological regimes (as summarized by Olefeldt et al., 2013). At regional scales, such as in this study, it is useful to separate the domain into eco-regions which group regions with similar vegetation, elevation, soil type, and soil moisture dynamics. One can then use the different eco-regions as a basis set of independent sources and sinks in a linear inversion. The eco-regions used within this study were taken from the Environmental Protection Agency's Level II map of eco-regions and grouped into the three following land types: tundra, which includes "Alaska Tundra"; boreal, which includes "Alaska Boreal Interior" and "Taiga Cordillera"; and mountains, which includes "Brooks Range Tundra", "Marine West Coast Forest", and "Boreal Cordillera" (Commission for Environmental Cooperation, 1997) (see Fig. 1). While "Marine West Coast Forests" are not mountainous by definition, a study of CH$_4$ fluxes north of 50° N identified heavily forested areas as being negligible sinks of CH$_4$ (Olefeldt et al., 2013). Therefore these forests are suitably grouped with mountains under the assumption that footprint sensitivity from these areas did not affect observed ΔCH$_4$. By using these predefined maps, we are attributing all net emissions to biogenic sources.
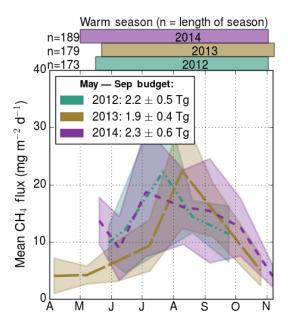
By calculating the mean fraction of the influence of each eco-region on our measurements using the footprint sensitivity maps, it is possible to estimate the net CH$_4$ flux from each eco-region using multiple linear least-squares regression according to the following:

$$\hat{E} = \sum_i f_i E_i, \tag{5}$$

where f_i are the fractions of influence from different eco-regions, $\hat{E}$ are the uniform CH$_4$ flux estimates, and E_i are the CH$_4$ fluxes from each eco-region. These estimates were grouped by month across all 3 years to maintain a sufficient sample size. To test the assumption that emissions from the mountain land type negligibly affected ΔCH$_4$, CH$_4$ flux was estimated with and without the mountain land type and presented in Sect. 4.4.2.

3.6 Regression analysis

To explore how the variability in CH$_4$ flux estimates is related to ecological, biological, and hydrological parameters, the footprint sensitivity functions were also used to calculate weighted means of different variables common in process-based models of CH$_4$ flux. Maps that were included in this analysis were surface, 10 and 40 cm daily soil temperature

Figure 4. Monthly-mean CH$_4$ flux estimates. Values are centered on the mean measurement date for a given month, and the shaded regions are the standard deviations of the individual flux estimates weighted by the 95 % CI for each estimate. See text for additional details. The bar plot above the graph marks the days when average soil temperatures from NARR were above zero, with the total number of unthawed days given by n.

(T_x, where x is the depth, K), and liquid soil moisture content (S_x, no unit) from the North American Regional Reanalysis (NARR) project (Mesinger et al., 2006); digital elevation (z, m) from ASTER; days since thaw (DST), derived from passive microwave satellite observations of surface thaw (Steiner et al., 2015); wetlands (%) (Bergamaschi et al., 2007); 30 and 100 cm soil organic carbon content (C_x, kg m^{-2}) from the Northern Circumpolar Soil Carbon Database (NCSCD) (Hugelius et al., 2013); and percent of soils classed as turbels, histels, gelisols, or non-soils from NCSCD (Hugelius et al., 2013).

Previous correlation analyses have suggested that CH$_4$ flux varies non-linearly with variables such as soil temperature (Yvon-Durocher et al., 2014) and elevation (Karion et al., 2016). As such, the following functional forms were used to characterize variability in CH$_4$ flux:

$$E = e^{f(x)} \tag{6}$$

$$f(x) = \begin{cases} E_a(\frac{1}{k\overline{x}} - \frac{1}{kx}), & \text{Boltzmann–Arrhenius type} \\ (\frac{1}{x+\overline{x}}), & \text{Inverse type} \\ (x - \overline{x}), & \text{Linear type} \end{cases} \tag{7}$$

where E is CH$_4$ flux, x is a hypothesized predictor variable, eV is the value of an electron volt in Joules (1.602×10^{-19} J), k is the Boltzmann constant (1.38×10^{-23} J K^{-1}), and $\overline{x}$ represents the mean sampled value of x. This transformation of units is performed such that when the predictor variable is

soil temperature, the fitted parameter optimizes the activation energy (E_a) in units of eV (Yvon-Durocher et al., 2014).

Multi-variable fits were also performed using an equation of the following form:

$$\hat{E} = e^{f(\mathbf{Z})\boldsymbol{\beta}}, \tag{8}$$

where $\hat{E}$ is an $N \cdot 1$ vector of modelled CH$_4$ flux estimates, $\mathbf{Z}$ is an $N \cdot (M+1)$ matrix with M columns of predictor variables transformed by $f(x)$ and one column of ones, and $\hat{\boldsymbol{\beta}}$ is an $(M+1) \cdot 1$ vector of estimated parameters. We searched through all possible combinations of functional forms by allowing the M columns of $\mathbf{Z}$ to take either the Boltzmann–Arrhenius, inverse, or linear forms written in Eq. (7), leaving the column of ones to fit a constant. The parameter vector $\hat{\boldsymbol{\beta}}$ is then constrained using the Levenberg–Marquardt algorithm for non-linear least-squares regression. Subsets of the data ($n < N$) were also fit to explore behaviour in limiting spatial and temporal cases. The best fit for each subset was chosen if it minimized the Aikake information criterion (AIC) (Burnham et al., 2011).

The footprint sensitivities are cumulative over 5 days, causing CH$_4$ flux estimates from individual profiles to represent 5-day averages (see Sect. 3.1 and 3.4). Regression analysis using the CH$_4$ fluxes estimated from individual profiles resulted in a lot of noise, and the majority of the environmental drivers could not explain the variability in these estimated CH$_4$ fluxes. To compensate for this, CH$_4$ flux estimates were first averaged into 5-day bins before fitting to reduce issues of autocorrelation and to generate independent estimates of CH$_4$ flux. As with the monthly-mean estimates, these were weighted by the total footprint influence. This temporal averaging reduced the total number of independent estimates used in the regression from 146 to 68, thus reducing the reliability of these results. It should be emphasized that the regression analyses are only reflective of seasonal variations on timescales of 5 days.

3.7 Uncertainties

Uncertainties in the estimated CH$_4$ flux from individual profiles were determined through bootstrapping both observational measurements and the integrated model footprints involved in its calculation by sampling each variable with replacement 500 times. Explicit variables included were as follows: (1) matching observations of CH$_4$, T, P, and P_w at each 250 m altitude bin to estimate uncertainties associated with the observations and spatial variability; (2) the footprint sensitivity at each 250 m altitude bin, approximating the uncertainty of releasing particles within neighbouring grid cells – it should be emphasized that this is not a true posterior variability and may underestimate full modelling uncertainties, although it is still a useful approximation of a type of model uncertainty; (3) the mixed layer height, which we varied by ±250 m and propagated through our calculations of $\hat{E}$ by either adding or removing another 250 m bin to the

integration in Eq. (2) but not changing $[CH_4]_0$, representing the uncertainty due to h; (4) same as (3) but changing $[CH_4]_0$ and representing the uncertainty due to $[CH_4]_0$; and (5) all of the above propagated through the entire calculation, representing the total methodological uncertainty in our calculations of CH_4. The 95 % confidence interval (CI) of the last step was used to estimate the uncertainty associated with the estimated CH_4 flux from individual profiles. The mean, minimum, and maximum 95 % CI (2.5–97.5 percentile) for each of these steps is shown in Table S4. They reveal that the largest methodological uncertainty associated with the results is the combined uncertainty in identifying both the mixed layer height and the $[CH_4]$ background.
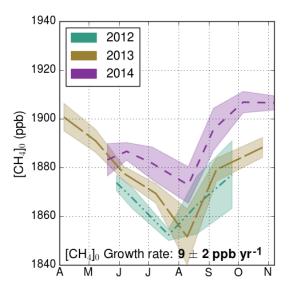
Uncertainties in the monthly-mean CH_4 flux were estimated in four ways: *average uncertainty*, the 95 % CI for each individual estimate is averaged for each month with no weighting; *weighted average uncertainty*, the 95 % CI for each individual estimate is averaged for each month and weighted by the column-integrated total surface influence (ΔI); *standard deviation*, the normal standard deviation is calculated from the residuals of the weighted monthly mean; and *weighted standard deviation*, the standard deviation of all CH_4 flux estimates within a given month is calculated, weighting each residual by ΔI and the inverse of the square of the 95 % CI. We present uncertainties calculated using the weighted standard deviation, because it accounts for both monthly variability and the uncertainty in the flux estimated from each profile. Results estimated using the average uncertainty were slightly lower, likely because they do not account for the variability in a given month. Uncertainties in the budget are propagated from the average monthly flux uncertainty by quadrature. For reference, uncertainties in the budget and monthly-mean estimates calculated using all four methods are shown in Table S4.

4 Results & discussion

In the following sections, we present estimates of regionally averaged monthly net CH_4 flux and the net total CH_4 emitted from our study domain from May to September. A discussion of the source of uncertainties in determining $[CH_4]_0$ will follow. Finally, the set of CH_4 fluxes estimated across 2012–2014 will be used to motivate discussions of how sampling different eco-regions across a dynamic range of soil conditions (e.g. soil temperature, soil moisture, soil type) affected the estimated CH_4 flux and budget.

4.1 CH4 flux estimates

Using the methods described in Sect. 3.4, monthly-mean net CH_4 fluxes for 2012–2014 were estimated from individual aircraft profiles of the atmosphere (Fig. 4). As will be shown in Sect. 4.4, we found that footprint sensitivity from oceans and mountains was poorly correlated with observations of

Figure 5. The mean tropospheric $[CH_4]_0$ estimated from profiles (shaded areas indicate 1σ). Values are centered on the mean measurement date.

ΔCH_4. Therefore, the estimated fluxes presented in this subsection only attributed CH_4 flux to the boreal and tundra eco-regions defined in Sect. 3.5. These estimates ranged from 2 to 36 mg CH_4 m^{-2} d^{-1} (2.5–97.5 % percentile) for individual profiles and showed a distinct seasonal cycle that peaked in late July or early August across all years (Fig. S1). Figure S2 illustrates that the residuals of the estimated net flux from individual profiles from the monthly mean are normally distributed, suggesting that our monthly-mean estimates are not strongly biased. Overall, our results are consistent with tall and eddy-covariance tower studies (e.g. Karion et al., 2016; Zona et al., 2016; Sweeney et al., 2016) and provide observational evidence that region-wide CH_4 flux may be, on average, as high as 5 mg m^{-2} d^{-1} in the colder months of April and November, also consistent with previous studies on the North Slope (Zona et al., 2016) and interior (Karion et al., 2016) of Alaska.

Monthly-mean flux estimates were found to be higher than those inferred from the CARVE tall tower near Fairbanks for the same months (3–9 mg CH_4 m^{-2} d^{-1}) (Karion et al., 2016), although the ranges from the two studies overlap. As discussed by Karion et al. (2016), the tower observations likely underestimate CH_4 flux compared to the aircraft observations because of the aircraft's increased sensitivity to the North Slope and southwestern Alaska, regions that are known to be seasonal wetlands (and therefore a significant CH_4 source, Bergamaschi et al., 2007), compared to the interior sites which were more sensitive to upland regions that are thought to emit less CH_4 (Olefeldt et al., 2013).

4.2 CH$_4$ budget calculations

Integrating over the months sampled every year (May–September), we estimate CH$_4$ emissions from our study region to be 2.2 ± 0.5 Tg, 1.9 ± 0.4 Tg, and 2.3 ± 0.6 Tg for 2012, 2013, and 2014, respectively, with the assumption that all non-mountainous land surfaces emit at a uniform rate over the entire month. As our observations do not extend throughout the colder months, we do not provide annual budget estimates since other studies have found that significant emissions of CH$_4$ are observed in the shoulder and cold seasons (Zona et al., 2016; Sweeney et al., 2016; Karion et al., 2016).

Previous estimates of emissions from Alaska during the growing season include the study by Chang et al. (2014), who used a similar method to estimate the May–September 2012 emissions to be 2.1 ± 0.5 Tg, as well as the geostatistical inversion of the CARVE observations by Miller et al. (2016), who estimated May–October CH$_4$ emissions of 1.80 ± 0.45, 1.65 ± 0.43, and 1.77 ± 0.45 Tg CH$_4$ for 2012, 2013, and 2014, respectively. Our mean estimates are within the uncertainties of these other studies, especially when we account for the $\sim 20\%$ greater area in our study domain. It is promising that our relatively simple method for calculating budgets using selected profiles from the CARVE aircraft observations arrives at similar estimates to values derived from the much more complex geostatistical inverse model used by Miller et al. (2016), particularly as their study was constrained by all the aircraft observations as well as hourly-averaged observations from the CRV tower.

Our estimates of May–September net CH$_4$ flux have a mean of 2.1 ± 0.5 Tg and show no significant difference over the 3 years. These results are consistent with the findings reported by Miller et al. (2016), who suggest that regional CH$_4$ emissions would require decades to respond to changes in surface conditions. Similarly, a recent analysis of long-term measurements of CH$_4$ flux on the North Slope in Alaska observed little change in boundary layer CH$_4$ enhancement over the past 29 years, despite increases in air temperature (Sweeney et al., 2016). This lack of trend could potentially be related to methanogen community structure in the Arctic, as recent microbiological research has found that communities from Arctic soils that were incubated at lower temperatures were insensitive to substrate manipulations, indicating that Arctic methanogens may not be sensitive to the addition of new labile carbon from thawing permafrost (Blake et al., 2015). While it is true that local-scale permafrost degradation patterns such as thermokarsts can result in local CH$_4$ fluxes of > 100 mg m^{-2} d^{-1} (Johnston et al., 2014), multi-decadal studies such as Sweeney et al. (2016) suggest that at a regional scale, CH$_4$ fluxes in Alaska have been stable.

4.3 CH$_4$ background estimates

4.3.1 Comparison of background CH$_4$

Our calculations of ΔCH$_4$ rely on the free tropospheric [CH$_4$] to represent background [CH$_4$] in the mixed layer. It is possible that the transport history of the free troposphere is different than that of the mixed layer. In this case, [CH$_4$] measured in the free troposphere would not be representative of the background at the surface. To assess the accuracy of our estimates of the [CH$_4$] background, we compare our free tropospheric values to in situ observations of the boundary layer CH$_4$ background observed at the Barrow Observatory ground station (BRW: 71.3° N, 156.6° W) in 2013 and 2014 (Dlugogencky, 2016). Because the station did not measure [CH$_4$] in 2012 (Sweeney et al., 2016), we instead compared the 2012 CARVE [CH$_4$]$_0$ estimates to the free tropospheric backgrounds measured monthly by aircraft at the Poker Flat site in interior Alaska (Global Monitoring Division, 2016). We also compared our estimate of the [CH$_4$] background to the backgrounds determined by Karion et al. (2016) for the CRV tower, who traced sampled air masses backward until they reached a boundary curtain at 170° W. Figure S3 shows that these other estimates of CH$_4$ background levels were generally within the standard deviation of [CH$_4$]$_0$ estimated from the CARVE profiles (± 8 ppb in 2012 and ± 6 ppb in 2013 and 2014). The exceptions were August 2013 and May 2014 when the CARVE observations were lower than the boundary layer CH$_4$ observed at BRW from the clean air sector, possibly resulting in an overestimation of CH$_4$ flux. It should be noted that the BRW site is located on the northern shore of Alaska and is separated from the Alaskan interior by the Brooks Range, so it is not always influenced by the same air mass that affects the remainder of the study region. As seen in Fig. 5, a distinct seasonal cycle in background [CH$_4$] is also evident and is consistent with cycles observed in the NOAA global CH$_4$ network (Dlugogencky, 2016). This gives us confidence that our calculated [CH$_4$]$_0$ is not strongly affected by changes in circulation due to long-range transport or stratospheric intrusion of clean air.

While the backgrounds estimated from the CRV tower for August 2013 are within our variability, the May 2014 background estimate from the CRV tower is between our estimate and the levels observed at BRW. To evaluate the magnitude of this effect on the estimated May–September budgets, the net CH$_4$ fluxes using the BRW ground station observations as our background were calculated for those 2 months, resulting in May–September budgets of 1.5 ± 0.2 and 1.8 ± 0.4 Tg CH$_4$ for 2013 and 2014, respectively. Since these values are within the uncertainties of our initial budget estimates and our background estimates correspond to those from the CRV tower, we believe that our estimates of [CH$_4$]$_0$ are representative of background levels in the mixed layer.

4.3.2 CH$_4$ background growth rate

Across the entire campaign, the estimated [CH$_4$]$_0$ had a median and standard deviation of 1880 ± 20 ppb, and a distinct seasonal cycle with higher mole fractions in colder months than in warmer months (Fig. 5). This seasonal cycle is driven by large-scale transport and chemical oxidation and is consistent with observations from global [CH$_4$] observations (Dlugogencky, 2016). From Fig. 5, it is also evident that background CH$_4$ in the free troposphere rose from 2012–2014.
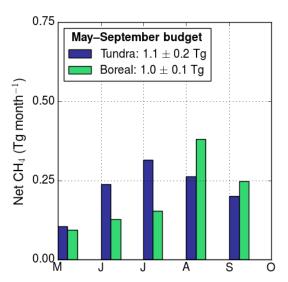
We estimate the atmospheric growth rate using monthly-mean CARVE-observed [CH$_4$]$_0$ fit to the function $y = \sum_{k=0}^{1} \sin(2\pi t + \frac{k\pi}{2}) + \sum_{k=0}^{1} t^k$, where time ($t$) is in units of years. This function is a simplified form of the function used by NOAA to estimate the global growth rate of CH$_4$ from their observation network (Earth Systems Research Laboratory , ESRL). Fitting with the Levenberg–Marquadt algorithm for non-linear least-squares, we estimate the atmospheric growth rate in the free troposphere over Alaska to be 9 ± 2 ppb yr^{-1} ($p < 0.001$) with a coefficient of determination of 0.77. The estimated growth rate is consistent with the 9 ± 1 ppb yr^{-1} and 8.6 ± 0.6 ppb yr^{-1} observed at Barrow (11 m a.s.l.) and Mauna Loa, HI (3397 m a.s.l.), respectively.

Overall we find that the monthly mean and annual growth rate determined from CARVE was the same as BRW within the variability of our observations, with the exception of a few months. These results indicate that the local mixed layer [CH$_4$]$_0$ in Alaska can be constrained from free tropospheric measurements and gives us confidence in our estimates of ΔCH$_4$.

4.4 Eco-region dynamics

4.4.1 Tundra & boreal eco-regions

Figure 6 shows the monthly emissions estimated for the tundra and boreal eco-regions over all 3 years estimated using the linear system in Eq. (5). The seasonal average CH$_4$ flux from tundra regions was 21 ± 3 mg m^{-2} d^{-1} and ranged from 6 to 34 mg m^{-2} d^{-1}. These estimates are comparable to flux observations in 2013–2014 from eddy-covariance towers on the North Slope, where the monthly-mean emissions from May to September ranged from 6 to 21 mg m^{-2} d^{-1} (Zona et al., 2016), as well as from the Yukon River Delta (25 mg m^{-2} d^{-1}) (Fan et al., 1992). However, our mean is lower and our range is narrower than those reported in a database of flux observations at the chamber-scale compiled by Olefeldt et al. (2013), who found that average net CH$_4$ flux from wet tundra north of 50° N was 64.5 mg m^{-2} d^{-1} and ranged between 31.9 and 100.6 mg m^{-2} d^{-1}. This is likely a result of our estimation method, which relies on a large degree of spatial and temporal averaging which smooths out the high CH$_4$ bursts that can be captured by flux chambers.
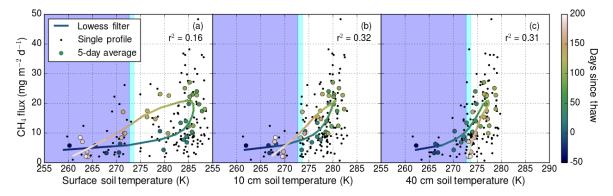

Figure 6. Estimated CH$_4$ emissions from tundra and boreal eco-regions averaged over all years.

The mean monthly flux was much lower in the boreal regions than in the tundra. On average it was 10 ± 2 mg m^{-2} d^{-1}, and ranged from 4 to 21 mg m^{-2} d^{-1}. This average is at the higher end of fluxes observed by an eddy covariance tower within a poorly drained forested region in Alaska, which found that CH$_4$ flux varied from 3 to 11 mg m^{-2} d^{-1} in the wettest regions (Iwata et al., 2015). However, it is reasonably similar to fluxes from the database by Olefeldt et al. (2013), which variously classified areas within the boreal region as bogs, fens and palsas, which emit on average 7–37 mg CH$_4$ m^{-2} d^{-1} (Olefeldt et al., 2013). Again, as with the tundra ecosystem, our spatial and temporal averaging method will smooth any CH$_4$ bursts.

Considering the period of May–September, the total flux from both ecosystems (2.2 ± 0.2 Tg) was consistent with the mean of the net budget calculated in the previous section assuming the ecosystems were identical. This analysis also estimates that the tundra eco-region, which represented 18 % of the total study area, accounted for more than half of the total net flux. Nevertheless, emissions from boreal regions cannot be neglected in estimates of the regional budget since their spatial coverage is quite extensive.

In Fig. 6, emissions from boreal regions appear to lag behind tundra regions by 1 month. This offset could be due to a more rapid onset of the spring thaw in the tundra eco-region, with maps of the freeze–thaw state showing that this area thawed 4–5 days earlier than the boreal eco-region in 2013 and 2014 (Steiner et al., 2015). While this is less than 1 week, a study relating the date of thaw to the annual radiation budget estimated that a 4-day shift in freeze–thaw date alters the annual radiation budget by 250 MJ m^{-2}, significantly altering the early season budget (Stone et al., 2002). However, in 2012, the boreal eco-region actually thawed 9 days earlier than the tundra. Considering that fluxes calculated from

Figure 7. (a–c) CH$_4$ flux estimates from atmospheric profiles are shown versus footprint-weighted mean soil temperatures at different depths. The shaded background denotes when the soil temperature was at (cyan) or below (blue) the fusion point of water.

all years are included in this regression, it is not clear that the difference in the seasonal pattern could be explained by differences in thaw date alone. Instead, the difference in the seasonal cycle is more likely a result of the distribution of wetlands. Using a map of wetland extent, it is estimated that 30 % of the tundra eco-region can be classified as a seasonal wetland, while only 15 % of the boreal eco-region is similarly classified (Bergamaschi et al., 2007). As wetlands are defined by a near-surface water table, methanogenesis can begin when the depth of thaw is much shallower, resulting in CH$_4$ emissions that begin much earlier than in regions with a deeper water table. These results and those in Sect. 4.5 are dependent on the wetland map chosen for this analysis. A more in-depth comparison and evaluation of wetland maps in this region can be found in Miller et al. (2016). In Sect. 4.5, the effect of the water table on the relationship between temperature and net CH$_4$ flux is explored further.

4.4.2 Mountain & ocean eco-regions

Up to this point, we have made explicit reference to our assumption that net CH$_4$ flux only originates from either the tundra or boreal eco-regions defined in Fig. 1. We tested this assumption by performing the same eco-region regression but included all surfaces: tundra, boreal, mountain, and ocean regions.

Regression analysis from these calculations found that oceans were a weak CH$_4$ source, emitting an average 2 ± 1 mg m^{-2} d^{-1} across the study months. However, Student t testing found that the fraction of oceans sampled had a consistently large p value across the season ($p > 0.05$), suggesting that footprint sensitivity in oceans was not correlated with ΔCH$_4$. This is consistent with a recent study of summertime sea–air flux of CH$_4$ around Svalbard, Norway, which measured low boundary layer CH$_4$ enhancements despite substantial surface ocean concentrations of CH$_4$ from subsea clathrate deposits in the high Arctic (Myhre et al., 2016).

Table 1. Correlation coefficients and predictors of CH$_4$ emissions for various linear regression models. Boltz.-Arrh.: Boltzmann–Arrhenius function. Inv.: inverse. Lin.: linear.

N	Subset condition	r^2	Predictors	Type
		All		
68	–	0.36	T_{40}, Z	Boltz.-Arrh., Inv.
		Subsets		
27	Wetlands Present	0.40	T_{10}, S_{10}	Boltz.-Arrh., Lin.
28	Wetlands Absent	0.48	T_{40}, S_{40}	Boltz.-Arrh., Lin.

T_X: mean sampled x cm subsoil temperature from NARR (K); S_X: mean sampled x cm subsoil liquid moisture fraction from NARR (–); Z: soil surface elevation above sea level (km).

Results from this regression also indicate that mountains might act as a weak seasonal sink of CH$_4$, with a mean strength of -1 ± 2 mg m^{-2} d^{-1}, consistent with recent regional observations of CH$_4$ in the mineral soils of Greenland (Jørgensen et al., 2015). However, the statistics ($p > 0.1$) were again too weak to confirm this as a regional-scale phenomenon in our study region. In light of these results, the oceans and mountains were masked from CH$_4$ flux estimates, as their inclusion would have led to an underestimation of the net CH$_4$ flux attributed to non-mountainous land surfaces.

4.5 Temperature dependence of CH$_4$ flux

The results of the regression analysis described in Sect. 3.6 are listed in Table 1 and indicate the r^2 of the best model, the driving variables, and the functional type for each subset (see Eq. 7). Overall, net CH$_4$ flux was seen to most strongly correlate to variance in a Boltzmann–Arrhenius function of T_{40} and the inverse of elevation ($r^2 = 0.36$). While these relationships have been observed in our study region in the past, primarily at the smaller scales of chambers and eddy-covariance towers (e.g. Olefeldt et al., 2013; Sturtevant et al., 2012; Zona et al., 2016), far fewer studies have reported them at a regional scale (Miller et al., 2016; Karion et al.,

2016). These latter analyses also identified the inverse elevation (Karion et al., 2016) and subsurface temperatures (Miller et al., 2016) to be important in explaining the variance of observed CH$_4$. As in the work of Karion et al. (2016), we used a relatively simple analysis method to arrive at similar explanatory variables than the more sophisticated geostatistical inversion model used by Miller et al. (2016) but with only a subset of the data. Although the r^2 from our analysis may seem low, they are comparable to values derived from regression analysis conducted for chamber studies (Olefeldt et al., 2013). Our results suggest that soil conditions that affect CH$_4$ flux at the more local scale are also relevant at regional scales.

Since both CH$_4$ production and flux can be much stronger in wetlands, (e.g. Olefeldt et al., 2013; Sturtevant et al., 2012), the profiles were subdivided into two groups based on the sensitivity of the profiles to wetlands in the domain. When a profile's footprint sensitivity was $\geq 20\%$ wetland by area, the profile was categorized as "Wetland Present". Conversely, profiles which had sensitivities $\leq 10\%$ to wetlands by area were categorized as "Wetland Absent". The percent of wetland per area sampled by a profile was calculated by averaging a map of wetland fraction (Bergamaschi et al., 2007) weighted by the footprint sensitivity. It was found that for profiles in the Wetlands Absent category, soil temperature and soil moisture at 40 cm soil depth were the key predictors in understanding the variability in net CH$_4$ flux ($r^2 = 0.48$), suggesting that CH$_4$ was being formed deeper in the soil column. By contrast, net CH$_4$ flux was best correlated with T_{10} and S_{10} ($r^2 = 0.40$) for profiles in the Wetland Present category.

These two regressions highlight the importance of understanding the depth at which methanogenesis (and methanotrophy) occurs. For instance, in non-wetlands, the water table is deeper than in wetlands. As a result, the onset of CH$_4$ production in non-wetland regions can significantly lag wetland areas, as the lower section of the soil column will take much longer to thaw. In fact, maps of soil temperature from NARR estimate that, on average, soil at 10 cm in the Wetland Present region thawed nearly 3 weeks before soil at 40 cm in the Wetland Absent regions (Mesinger et al., 2006). In addition, soils at these depths and in these regions warmed very differently: T_{10} in the Wetland Present regions increased at an average rate of 0.10 K day^{-1} from point of thaw to the point of annual maximum, while T_{40} in the Wetland Absent regions increased by only 0.06 K day^{-1}. While CH$_4$ production may occur at any depth within an inundated soil column, CH$_4$ produced at lower soil depths can be transport limited (depending on bubble formation or aerenchyma); it is, therefore, intuitive that CH$_4$ produced in wetlands will be more directly correlated to differences in temperature near the surface. Similarly, the dependence of CH$_4$ production (and ultimately, CH$_4$ flux) on soil moisture will be most pronounced just beneath the water table, where soil moisture is more susceptible to variability than at lower depths.

The freeze–thaw processes and soil microphysics discussed above can be extended to explain the seasonal cycles presented in both Figs. 4 and 6. First, as remarked in Sect. 4.4.1, the tundra eco-region possesses more wetland extent than the boreal. As a result, the delayed thaw of the 40 cm soil in combination with slower warming likely explains the delay in boreal eco-region CH$_4$ flux. Second, while maps of footprint sensitivity across all years showed relatively consistent sensitivity to the tundra in the west and southwest of Alaska (see Figs. 1 and 2), they showed that our 2012 measurements were more sensitive to the North Slope of Alaska relative to the boreal eco-region than in other years. On average, ~ 30, 20, and 20 % of the footprint sensitivity was from regions classified as tundra in 2012, 2013, and 2014, respectively. Since the tundra region possesses more seasonal wetlands, it is therefore not surprising that the 2012 seasonal cycle of net CH$_4$ flux in Fig. 4 closely resembles the tundra eco-region in Fig. 6. However, as the tundra only represents 18 % of the total area of interest, it is likely that the sampling in 2013 and 2014 sampled the eco-regions more evenly with respect to their total area, while the sampling in 2012 may have been over-sensitive to the tundra. In particular, if we consider that early season flux in 2014 is identical to that in 2012, it is obvious that soil moisture is not the only variable at play. In fact, seasonal cycles of domain-average subsurface temperature from NARR are very nearly identical in timing to the seasonal cycles observed in CH$_4$ flux. To highlight this timing, the start of the warm season shown in Fig. 4 was defined as the day when domain-averaged soil temperatures at 40 cm exceeded 273 K. In this respect, the early season of 2012 and 2014 may be more similar than previously thought. Since we postulate that CH$_4$ flux is occurring at 40 cm within the boreal eco-region, which is larger by area and more heavily sampled by the campaign, it is not surprising that domain-average CH$_4$ flux rises at the same rate in the spring of 2012 and 2014, while showing significant delay in 2013.

Overall, subsurface soil temperature was seen to be the single best explanatory variable throughout the regression analysis. Following the work of Zona et al. (2016), the seasonal cycles of CH$_4$ flux are plotted versus soil temperature and coloured by days since the thaw in Fig. 7. In this figure, CH$_4$ flux estimates from individual profiles are shown in black points. To highlight the average seasonal trend, these individual estimates were block-averaged into 5-day bins of DST based on satellite retrievals of thaw state (coloured points), before being smoothed by a lowess filter which locally averaged 35 %, or 80 days, of the seasonal cycle (coloured line) (Steiner et al., 2015). Flux estimates from May 2014 were suspected of being overestimated (Sect. 4.3.1) and were thus excluded from this analysis.

Of the three depths presented in Fig. 7, the seasonal cycle of CH$_4$ flux has the most consistent, monotonic relationship with T_{40} throughout the study, while the other depths, especially the individual profiles (small black points) show

more scatter. We conjecture that the monotonicity of the relationship between T_{40} and CH$_4$ we observe for our study region is reflective of the fact that CH$_4$ production is, on average, taking place near this soil level. Evidence for the production of CH$_4$ at soil depths well below the surface have been reported at the eddy-covariance scale before. In particular, the counterclockwise hysteresis loop in our observations of T_{10} and CH$_4$ flux is very similar to the relationship observed by eddy-covariance towers at Ivotuk between CH$_4$ and T_{15} (Zona et al., 2016). Whereas observations of CH$_4$ flux in wetland sites exhibited a clockwise hysteresis loop, the Ivotuk site itself was much drier than other eddy-covariance sites compared in the study, leading the authors to conclude that the direction of the loop was related to whether CH$_4$ production was occurring above (clockwise) or below (counterclockwise) the soil depth at which temperature was measured (Zona et al., 2016). Similarly, an eddy-covariance tower near Fairbanks, AK, also observed a counterclockwise hysteresis loop when CH$_4$ flux was plotted against T_{20} (Iwata et al., 2015). It is, therefore, reasonable to believe that CH$_4$ production is occurring at depths of ~ 40 cm in the broader Wetland Absent regions as a result of a lower water table. In particular, these drier regions play a large role in the late season (September–December) budget, as the production of CH$_4$ at soil depths well beneath the surface enables CH$_4$ flux to continue even after the surface soil has begun to freeze (Zona et al., 2016). In the specific case of Ivotuk, CH$_4$ emitted after the surface had frozen represented nearly 30 % of the total annual budget (Zona et al., 2016). Since Wetland Absent regions make up 50 % of the surface area of the tundra and boreal eco-regions, it is important that these regions are not overlooked when modelling CH$_4$ emissions at a regional scale.

From Fig. 7, we fit the mean CH$_4$ flux and T_{40} from the 5-day means to a Boltzmann–Arrhenius equation and determined an activation energy of 0.75 ± 0.20 eV. This value is slightly lower than, but still within uncertainties of, the global mean activation energy of 0.96 eV (0.86–1.07 eV, 95 % CI), calculated using CH$_4$ flux measurements from static chambers (Yvon-Durocher et al., 2014). Using T_{40} from NARR in this parameterization, we estimate May–September emissions from our study region to be 2.1 ± 0.3 Tg, 1.8 ± 0.3 Tg and 2.0 ± 0.3 Tg for 2012, 2013, and 2014, respectively (only integrating over non-mountainous areas). This simple model does a remarkable job of capturing the growing season budget estimated from the aircraft observations as well as the timing of the peak in CH$_4$ emissions. As more winter-time measurements would be necessary to properly constrain cold season fluxes, estimates of total annual budgets based on this model are not reported.

5   Conclusions

Analysis of CH$_4$ column enhancements supplemented by simulated atmospheric transport allowed us to estimate the monthly-mean CH$_4$ fluxes from our study domain (50–75° N, 130–170° W). We estimate that domain-averaged net CH$_4$ flux from May to September ranged from 2.0 to 36 mg m^{-2} d^{-1} and that 2.2 ± 0.5 Tg, 1.9 ± 0.4 Tg, and 2.3 ± 0.6 Tg CH$_4$ were emitted from our domain for 2012, 2013, and 2014, respectively. These estimates were consistent with more complex statistical methods, indicating that this relatively simple analytical technique, with only a subset of the data, is sufficient for determining regional-scale CH$_4$ emissions. The methodology and analysis that followed are therefore useful guidelines for regional monitoring programs which suggest that short, regular profiling of different eco-regions supplemented by fine-scale meteorological modelling can be sufficient to characterize the regional dynamics of the carbon cycle.

Despite the lack of spatial resolution within the CH$_4$ flux estimates, we were able to leverage the atmospheric transport model to inform some basic regression models on how CH$_4$ flux co-varied with different soil variables and characteristics. We found that when we sampled wetlands, CH$_4$ flux co-varied most significantly with T_{10}. Conversely, when wetlands were absent, CH$_4$ flux co-varied with T_{40}. These two results are consistent with observations of how the water table affects the anaerobic production of CH$_4$ at small spatial scales and emphasize that it is a relevant control at regional scales. Across our study region, we were able to reasonably predict the May–September CH$_4$ budget using a Boltzmann–Arrhenius model relating CH$_4$ flux to T_{40}.

Overall, these regressions provide insight into the differences in seasonal cycles observed across the years and eco-regions. Methanogenesis in wetlands (like the tundra) occur closer to the surface since the water table depth is higher. By contrast, methanogenesis occurs lower in the soil column in regions with fewer wetlands (such as boreal regions). Since surface soils will thaw earlier in the season than deeper soils, CH$_4$ production begins earlier in wetland regions and ends later in drier regions. As a result, campaigns like CARVE, who sample across eco-regions, need to be cautious to evenly sample regions with different subsurface hydrology. Overall our results show that factors found to affect CH$_4$ emissions at scales of 1 m to 1 km are still relevant at the regional scale, suggesting that regional emissions can be determined by upscaling local-scale studies.

The measurements of trace gas mixing ratios and thermodynamic properties used to form the atmospheric profiles are available via ORNL DAAC at https://doi.org/10.3334/ORNLDAAC/1402 (Budney et al., 2016).

The maps of footprint influence related to the above mixing ratios are available via ORNL DAAC at https://doi.org/10.3334/ORNLDAAC/1431 (Henderson et al., 2017).

Maps of freeze–thaw state used to derive the average day since thaw of a footprint are available via ORNL DAAC at https://doi.org/10.3334/ORNLDAAC/1383 (Steiner et al., 2017).

NARR data were provided by the NOAA/OAR/ESRL PSD, Boulder, Colorado, USA, from their web site: ftp://ftp.cdc.noaa.gov/Datasets/NARR/subsurface/ (NOAA, 2017).

NCSCD data were provided from Stockholm University on behalf of the Bolin Centre for Climate Research (2017) via their web site: http://bolin.su.se/data/ncscd/.

The Supplement related to this article is available online at https://doi.org/10.5194/acp-18-185-2018-supplement.

References

Bean, B. R. and Dutton, E.: Radio meteorology, Dover Publications, 1966.

Bergamaschi, P., Frankenberg, C., Meirink, J., Krol, M., Dentener, F., Wagner, T., Platt, U., Kaplan, J., Körner, S., Heimann, M., Dlugokencky, E., and Goede, A.: Satellite chartography of atmospheric methane from SCIAMACHY on board ENVISAT: 2. Evaluation based on inverse model simulations, J. Geophys. Res.-Atmos., 112, https://doi.org/10.1029/2006JD007268, 2007.

Bergamaschi, P., Houweling, S., Segers, A., Krol, M., Frankenberg, C., Scheepmaker, R. A., Dlugokencky, E., Wofsy, S. C., Kort, E. A., Sweeney, C., Schuck, T., Brenninkmeijer, C., Chen, H., Beck, V., and Gerbig, C.: Atmospheric CH$_4$ in the first decade of the 21st century: Inverse modeling analysis using SCIAMACHY satellite retrievals and NOAA surface measurements, J. Geophys. Res., 118, 7350–7369, https://doi.org/10.1002/jgrd.50480, 2013.

Blake, L., Ovreas, L., Head, I., and Gray, N.: Response of Methanogens in Arctic Sediments to and Methanogenic Substrate Availability, PLoS ONE, 10, e0129733, https://doi.org/10.1371/journal.pone.0129733, 2015.

Bolin Centre for Climate Research: NCSCD data, available at: http://bolin.su.se/data/ncscd/, last access: 24 November 2017.

Bromwich, D. H., Hines, K. M., and Bai, L.: Development and testing of Polar Weather Research and Forecasting model: 2. Arctic Ocean, J. Geophys. Res., 114, D08122, https://doi.org/10.1029/2008JD010300, 2009.

Budney, J. W., Chang, R. Y.-W., Commane, R., Daube, B. C., Dayalu, A., Dinardo, S. J., Gottlieb, E. W., Karion, A., Lindaas, J. O. W., Miller, C. E., Miller, J. B., Miller, S., Pender, M., Pittman, J. V., Samra, J., Sweeney, C., Wofsy, S. C., and Xiang, B.: CARVE: L2 Merged Atmospheric CO$_2$, CO, O$_3$ and CH$_4$ Concentrations, Alaska, 2012–2015, ORNL DAAC, Oak Ridge, Tennessee, USA, available at: https://doi.org/10.3334/ORNLDAAC/1402 (last access: 1 January 2017), 2016.

Bruhwiler, L., Dlugokencky, E., Masarie, K., Ishizawa, M., Andrews, A., Miller, J., Sweeney, C., Tans, P., and Worthy, D.: CarbonTracker-CH$_4$: an assimilation system for estimating emissions of atmospheric methane, Atmos. Chem. Phys., 14, 8269–8293, https://doi.org/10.5194/acp-14-8269-2014, 2014.

Burnham, K. P., Anderson, D. R., and Huyvaert, K. P.: AIC model selection and multimodel inference in behavioral ecology: some background, observations, and comparisons, Behav. Ecol. Sociobiol., 65, 23–35, 2011.

Chan, K. M. and Wood, R.: The seasonal cycle of planetary boundary layer depth determined using COSMIC radio occultation data, J. Geophys. Res.-Atmos., 118, 12422–12434, https://doi.org/10.1002/2013JD020147, 2013.

Chang, R. Y.-W., Miller, C. E., Dinardo, S. J., Karion, A., Sweeney, C., Daube, B. C., Henderson, J. M., Mountain, M. E., Eluszkiewicz, J., Miller, J. B., Bruhwiler, L. M. P., and Wofsy, S. C.: Methane emissions from Alaska in 2012 from CARVE airborne observations, P. Natl. Acad. Sci. USA, 111, 16694–16699, 2014.

Chen, H., Winderlich, J., Gerbig, C., Hoefer, A., Rella, C. W., Crosson, E. R., Van Pelt, A. D., Steinbach, J., Kolle, O., Beck, V., Daube, B. C., Gottlieb, E. W., Chow, V. Y., Santoni, G. W., and Wofsy, S. C.: High-accuracy continuous airborne measurements of greenhouse gases (CO$_2$ and CH$_4$) using the cavity ring-down spectroscopy (CRDS) technique, Atmos. Meas. Tech., 3, 375–386, https://doi.org/10.5194/amt-3-375-2010, 2010.

Chen, Y.-H. and Prinn, R. G.: Estimation of atmospheric methane emissions between 1996 and 2001 using a three-dimensional global chemical transport model, J. Geophys. Res., 111, D10307, https://doi.org/10.1029/2005JD006058, 2006.

Chou, W. W., Wofsy, S. C., Harriss, R. C., Lin, J. C., Gerbig, C., and Sachse, G. W.: Net fluxes of CO$_2$ in Amazonia de-

rived from aircraft observations, J. Geophys. Res., 107, 4614, https://doi.org/10.1029/2001JD001295, 2002.

Christensen, T.: Methane emission from Arctic tundra, Biogeochemistry, 21, 117–139, https://doi.org/10.1007/BF00000874, 1993.

Ciais, P., Sabine, C., Bala, G., Bopp, L., Brovkin, V., Canadell, J., Chhabra, A., DeFries, R., Galloway, J., Heimann, M., Jones, C., Le Quéré, C., Myneni, R. B., Piao, S., and Thornton, P.: Carbon and other biogeochemical cycles, in: Climate change 2013: the physical science basis. Contribution of Working Group I to the Fifth Assessment Report of the Intergovernmental Panel on Climate Change, Cambridge University Press, 465–570, 2014.

Collins, M., Knutti, R., Arblaster, J., Dufresne, J.-L., Fichefet, T., Friedlingstein, P., Gao, X., Gutowski, W., Johns, T., Krinner, G., Shongwe, M., Tebaldi, C., Weaver, A., and Wehner, M.: Long-term Climate Change: Projections, Commitments and Irreversibility, book section 12, Cambridge University Press, Cambridge, United Kingdom and New York, NY, USA, 1029–1136, https://doi.org/10.1017/CBO9781107415324.024, 2013.

Commane, R., Lindaas, J., Benmergui, J., Luus, K. A., Chang, R. Y.-W., Daube, B. C., Euskirchen, E. S., Henderson, J. M., Karion, A., Miller, J. B., Miller, S. M., Parazoo, N. C., Randerson, J. T., Sweeney, C., Tans, P., Thoning, K., Veraverbeke, S., Miller, C. E., and Wofsy, S. C.: Carbon dioxide sources from Alaska driven by increasing early winter respiration from Arctic tundra, P. Natl. Acad. Sci. USA, 114, 5361–5366, https://doi.org/10.1073/pnas.1618567114, 2017.

Commission for Environmental Cooperation: Ecological regions of North America: toward a common perspective, Tech. rep., Commission for Environmental Cooperation, 1997.

Dlugogencky, E.: Trends in Atmospheric Methane, Tech. rep., National Oceanic and Atmospheric Administration, available at: www.esrl.noaa.gov/gmd/ccgg/trends_ch4/, last access: 1 July 2016.

Dlugokencky, E., Myers, R., Lang, P., Masarie, K., Crotwell, A., Thoning, K., Hall, B., Elkins, J., and Steele, L.: Conversion of NOAA atmospheric dry air CH$_4$ mole fractions to a gravimetrically prepared standard scale, J. Geophys. Res.-Atmos., 110, D18306, https://doi.org/10.1029/2005JD006035, 2005.

Dlugokencky, E. J., Nisbet, E. G., Fisher, R., and Lowry, D.: Global atmospheric methane: budget, changes and dangers, Philos. T. R. Soc. A, 369, 2058–2072, 2011.

Earth Systems Research Laboratory (ESRL): NOAA/ESRL calculation of global means, Tech. rep., National Oceanic and Atmospheric Administration, available at: http://www.esrl.noaa.gov/gmd/ccgg/about/global_means.html, last access: 1 July 2016.

Fan, S. M., Wofsy, S. C., Bakwin, P. S., Jacob, D. J., Anderson, S. M., Kebabian, P. L., McManus, J. B., and Kolb, C. E.: Micrometerological Measurements of CH$_4$ and CO$_2$ Exchange Between the Atmosphere and Subarctic Tundra, J. Geophys. Res., 97, 16627–16643, 1992.

Gatti, L. V., Gloor, M., Miller, J. B., Doughty, C. E., Malhi, Y., Domingues, L. G., Basso, L. S., Martinewski, a., Correia, C. S. C., Borges, V. F., Freitas, S., Braz, R., Anderson, L. O., Rocha, H., Grace, J., Phillips, O. L., and Lloyd, J.: Drought sensitivity of Amazonian carbon balance revealed by atmospheric measurements, Nature, 506, 76–80, https://doi.org/10.1038/nature12957, 2014.

Gerbig, C., Lin, J. C., Wofsy, S. C., Daube, B. C., Andrews, A. E., Stephens, B. B., Bakwin, P. S., and Grainger, C. A.: Toward constraining regional-scale fluxes of CO$_2$ with atmospheric observations over a continent: 2. Analysis of COBRA data using a receptor-oriented framework, J. Geophys. Res., 108, 4757, https://doi.org/10.1029/2003JD003770, 2003.

Global Monitoring Division: Carbon Cycle Greenhouse Gas Reference Network, Tech. rep., National Oceanic and Atmospheric Administration, available at: http://www.esrl.noaa.gov/gmd/dv/site/PFA.html, last access: 8 December 2016.

Hartery, S., Commane, R., Lindaas, J., Sweeney, C., Henderson, J., Mountain, M., Steiner, N., McDonald, K., Dinardo, S. J., Miller, C. E., Wofsy, S. C., and Chang, R. Y.-W.: CARVE: Ecosystem CH$_4$ Fluxes Derived From Aircraft Observations, Alaska 2012–2014, ORNL DAAC, Oak Ridge, Tennessee, USA, available at: http://dx.doi.org/10.3334/ORNLDAAC/1558, 2018.

Henderson, J. M., Eluszkiewicz, J., Mountain, M. E., Nehrkorn, T., Chang, R. Y.-W., Karion, A., Miller, J. B., Sweeney, C., Steiner, N., Wofsy, S. C., and Miller, C. E.: Atmospheric transport simulations in support of the Carbon in Arctic Reservoirs Vulnerability Experiment (CARVE), Atmos. Chem. Phys., 15, 4093–4116, https://doi.org/10.5194/acp-15-4093-2015, 2015.

Henderson, J., Miller, J. B., Nehrkorn, T., Chang, R. Y.-W., Sweeney, C., Steiner, N., Wofsy, S. C., and Miller, C. E.: CARVE: L4 Gridded Footprints from WRF-STILT model, 2012–2016, ORNL DAAC, Oak Ridge, Tennessee, USA, available at: https://doi.org/10.3334/ORNLDAAC/1431, last access: 1 January 2017.

Hines, K., Bromwich, D., Bai, L., Bitz, C., Powers, J., and Manning, K.: Sea ice enhancements to Polar WRF, Mon. Weather Rev., 143, 2363–2385, https://doi.org/10.1175/MWR-D-14-00344.1, 2015.

Hines, K. M. and Bromwich, D. H.: Development and Testing of Polar Weather Research and Forecasting (WRF) Model. Part I: Greenland Ice Sheet Meteorology, Mon. Weather Rev., 136, 1971–1989, https://doi.org/10.1175/2007MWR2112.1, 2008.

Hines, K. M., Bromwich, D. H., Bai, L.-S., Barlage, M., and Slater, A. G.: Development and Testing of Polar WRF. Part III: Arctic Land, J. Climate, 24, 26–48, https://doi.org/10.1175/2010JCLI3460.1, 2011.

Hugelius, G., Tarnocai, C., Broll, G., Canadell, J. G., Kuhry, P., and Swanson, D. K.: The Northern Circumpolar Soil Carbon Database: spatially distributed datasets of soil coverage and soil carbon storage in the northern permafrost regions, Earth Syst. Sci. Data, 5, 3–13, https://doi.org/10.5194/essd-5-3-2013, 2013.

Iwata, H., Harazono, Y., Ueyama, M., Sakabe, A., Nagano, H., Kosugi, Y., Takahashi, K., and Kim, Y.: Methane exchange in a poorly-drained black spruce forest over permafrost observed using the eddy covariance technique, Agr. Forest Meteorol., 214, 157–168, 2015.

Jenness, J. S.: Calculating landscape surface area from digital elevation models, Wildlife Soc. B., 32, 829–839, 2004.

Johnston, C. E., Ewing, S. A., Harden, J. W., Varner, R. K., Wickland, K. P., Koch, J. C., Fuller, C. C., Manies, K., and Jorgenson, M. T.: Effect of permafrost thaw on CO$_2$ and CH$_4$ exchange in a western Alaska peatland chronosequence, Environ. Res. Lett., 9, 085004, http://stacks.iop.org/1748-9326/9/i=8/a=085004, 2014.

Jørgensen, C. J., Johansen, K. M. L., Westergaard-Nielsen, A., and Elberling, B.: Net regional methane sink in High Arctic soils of northeast Greenland, Nat. Geosci., 8, 20–23, 2015.

Jorgenson, M. T., Shur, Y. L., and Pullman, E. R.: Abrupt increase in permafrost degradation in Arctic Alaska, Geophys. Res. Lett., 33, L02503, https://doi.org/10.1029/2005GL024960, 2006.

Karion, A., Sweeney, C., Wolter, S., Newberger, T., Chen, H., Andrews, A., Kofler, J., Neff, D., and Tans, P.: Long-term greenhouse gas measurements from aircraft, Atmos. Meas. Tech., 6, 511–526, https://doi.org/10.5194/amt-6-511-2013, 2013.

Karion, A., Sweeney, C., Miller, J. B., Andrews, A. E., Commane, R., Dinardo, S., Henderson, J. M., Lindaas, J., Lin, J. C., Luus, K. A., Newberger, T., Tans, P., Wofsy, S. C., Wolter, S., and Miller, C. E.: Investigating Alaskan methane and carbon dioxide fluxes using measurements from the CARVE tower, Atmos. Chem. Phys., 16, 5383–5398, https://doi.org/10.5194/acp-16-5383-2016, 2016.

Kirschke, S., Bousquet, P., Ciais, P., et al.: Three decades of global methane sources and sinks, Nat. Geosci., 6, 813–823, 2013.

Lin, J., Gerbig, C., Wofsy, S., Andrews, A., Daube, B., Davis, K., and Grainger, C.: A near-field tool for simulating the upstream influence of atmospheric observations: The Stochastic Time-Inverted Lagrangian Transport (STILT) model, J. Geophys. Res.-Atmos., 108, 4493, https://doi.org/10.1029/2002JD003161, 2003.

Mesinger, F., DiMego, G., Kalnay, E., Mitchell, K., Shafran, P. C., Ebisuzaki, W., Jović, D., Woollen, J., Rogers, E., Berbery, E. H., Ek, M. B., Fan, Y., Grumbine, R., Higgins, W., Li, H., Lin, Y., Manikin, G., Parrish, D., and Shi, W.: North American regional reanalysis, B. Am. Meteorol. Soc., 87, 343–360, 2006.

Miller, S., Miller, C., Commane, R., Chang, R.-W., Dinardo, S., Henderson, J., Karion, A., Lindaas, J., Melton, J., Miller, J., Sweeney, C., Wofsy, S., and Michalak, A.: A multi-year estimate of methane fluxes in Alaska from CARVE atmospheric observations, Global Biogeochem. Cy., 30, 1441–1453, https://doi.org/10.1002/2016GB005419, 2016.

Myhre, C. L., Ferré, B., Platt, S., Silyakova, A., Hermansen, O., Allen, G., Pisso, I., Schmidbauer, N., Stohl, A., Pitt, J., Jansson, P., Greinert, J., Percival, C., Fjaeraa, A. M., O'Shea, S. J., Gallagher, M., Le Breton, M., Bower, K. N., Bauguitte, S. J. B., Dalsøren, S., Vadakkepuliyambatta, S., Fisher, R. E., Nisbet, E. G., Lowry, D., Myhre, G., Pyle, J. A., Cain, M., and Mienert, J.: Extensive release of methane from Arctic seabed west of Svalbard during summer 2014 does not influence the atmosphere, Geophys. Res. Lett., 43, 4624–4631, 2016.

Nehrkorn, T., Eluszkiewicz, J., Wofsy, S. C., Lin, J. C., Gerbig, C., Longo, M., and Freitas, S.: Coupled weather research and forecasting–stochastic time-inverted lagrangian transport (WRF–STILT) model, Meteorol. Atmos. Phys., 107, 51–64, 2010.

NOAA: NARR data, available at: ftp://ftp.cdc.noaa.gov/Datasets/NARR/subsurface/, last access: 24 November 2017.

Novelli, P., Collins, J., Myers, R., Sachse, G., and Scheel, H.: Reevaluation of the NOAA/CMDL carbon monoxide reference scale and comparisons with CO reference gases at NASA-Langley and the Fraunhofer Institut, J. Geophys. Res.-Atmos., 99, 12833–12839, 1994.

Olefeldt, D., Turetsky, M. R., Crill, P. M., and McGuire, A. D.: Environmental and physical controls on northern terrestrial methane emissions across permafrost zones, Glob. Change Biol., 19, 589–603, 2013.

O'Shea, S. J., Allen, G., Gallagher, M. W., Bower, K., Illingworth, S. M., Muller, J. B. A., Jones, B. T., Percival, C. J., Bauguitte, S. J.-B., Cain, M., Warwick, N., Quiquet, A., Skiba, U., Drewer, J., Dinsmore, K., Nisbet, E. G., Lowry, D., Fisher, R. E., France, J. L., Aurela, M., Lohila, A., Hayman, G., George, C., Clark, D. B., Manning, A. J., Friend, A. D., and Pyle, J.: Methane and carbon dioxide fluxes and their regional scalability for the European Arctic wetlands during the MAMM project in summer 2012, Atmos. Chem. Phys., 14, 13159–13174, https://doi.org/10.5194/acp-14-13159-2014, 2014.

Osterkamp, T.: The recent warming of permafrost in Alaska, Global Planet. Change, 49, 187–202, 2005.

Overland, J., Hanna, E., Hanssen-Bauer, I., Kim, S.-J., Walsh, J., Wang, M., Bhatt, U., and Thoman, R.: Arctic Report Card 2015: Surface Air Temperatures, Tech. rep., National Oceanic and Atmospheric Administration, available at: http://www.arctic.noaa.gov/reportcard (last access: 1 January 2017), 2015.

Sasakawa, M., Shimoyama, K., Machida, T., Tsuda, N., Suto, H., Arshinov, M., Davydov, D., Fofonov, A., Krasnov, O., Saeki, T., Koyama, Y., and Maksyutov, S.: Continuous measurements of methane from a tower network over Siberia, Tellus B, 62, 403–416, https://doi.org/10.1111/j.1600-0889.2010.00494.x, 2010.

Schuur, E., McGuire, A., Schädel, C., Grosse, G., Harden, J., Hayes, D., Hugelius, G., Koven, C., Kuhry, P., Lawrence, D., Natali, S. M., Olefeldt, D., Romanovsky, V. E., Schaefer, K., Turetsky, M. R., Treat, C. C. and Vonk, J. E.: Climate change and the permafrost carbon feedback, Nature, 520, 171–179, 2015.

Skamarock, W., Klemp, J., Dudhia, J., Gill, D., Barker, D., Wang, X.-Y., Wang, W., and Powers, J.: A Description of the Advanced Research WRF Version 3, Tech. rep., MMM Division, NCAR, available at: http://www.mmm.ucar.edu/wrf/users/docs/arw_v3.pdf (last access: 1 January 2017), 475+STR, 2008.

Steiner, N., McDonald, K., Dinardo, S., and Miller, C.: Snowmelt and Surface Freeze/Thaw Timings over Alaska derived from Passive Microwave Observations using a Wavelet Classifier, American Geophysical Union, San Francisco, CA, 14–18 December 2015.

Steiner, N., McDonald, K. C., and Miller, C. E.: CARVE: Daily Thaw State of Boreal and Arctic Alaska from AMSR-E and SSM/I, 2003–2014, ORNL DAAC, Oak Ridge, Tennessee, USA, available at: https://doi.org/10.3334/ORNLDAAC/1383, last access: 1 January 2017.

Stone, R. S., Dutton, E. G., Harris, J. M., and Longenecker, D.: Earlier spring snowmelt in northern Alaska as an indicator of climate change, J. Geophys. Res.-Atmos., 107, https://doi.org/10.1029/2000JD000286, 2002.

Stull, R. B.: An introduction to boundary layer meteorology, vol. 13, Springer Science & Business Media, 1988.

Sturtevant, C. S., Oechel, W. C., Zona, D., Kim, Y., and Emerson, C. E.: Soil moisture control over autumn season methane flux, Arctic Coastal Plain of Alaska, Biogeosciences, 9, 1423–1440, https://doi.org/10.5194/bg-9-1423-2012, 2012.

Sweeney, C., Dlugokencky, E., Miller, C., Wofsy, S., Karion, A., Dinardo, S., Chang, R. Y.-W., Miller, J., Bruhwiler, L., Crotwell, A., Newberger, T., McKain, K. Stone, R. S., Wolter, S. E., Lang, P. E., and Tans, P.: No significant increase in long-term CH_4 emissions on North Slope of Alaska despite significant in-

crease in air temperature, Geophys. Res. Lett., 43, 6604–6611, https://doi.org/10.1002/2016GL069292, 2016.

Tarnocai, C., Canadell, J., Schuur, E., Kuhry, P., Mazhitova, G., and Zimov, S.: Soil organic carbon pools in the northern circumpolar permafrost region, Global Biogeochem. Cy., 23, GB2023, https://doi.org/10.1029/2008GB003327, 2009.

Whalen, S.: Biogeochemistry of methane exchange between natural wetlands and the atmosphere, Environ. Eng. Sci., 22, 73–94, 2005.

Xue, K., M. Yuan, M., J. Shi, Z., Qin, Y., Deng, Y., Cheng, L., Wu, L., He, Z., Van Nostrand, J. D., Bracho, R., Natali, S., Schuur, E. A. G., Luo, C., Konstantinidis, K. T., Wang, Q., Cole, J. R., Tiedje, J. M., Luo, Y., and Zhou, J.: Tundra soil carbon is vulnerable to rapid microbial decomposition under climate warming, Nature Climate Change, 6, 595–600, https://doi.org/10.1038/nclimate2940, 2016.

Yvon-Durocher, G., Allen, A. P., Bastviken, D., Conrad, R., Gudasz, C., St-Pierre, A., Thanh-Duc, N., and Del Giorgio, P. A.: Methane fluxes show consistent temperature dependence across microbial to ecosystem scales, Nature, 507, 488–491, 2014.

Zhang, J. and Rothrock, D.: Modeling global sea ice with a thickness and enthalpy distribution model in generalized curvilinear coordinates, Mon. Weather Rev., 131, 845–861, 2003.

Zhao, C. L. and Tans, P. P.: Estimating uncertainty of the WMO mole fraction scale for carbon dioxide in air, J. Geophys. Res.-Atmos., 111, D08S09, https://doi.org/10.1029/2005JD006003, 2006.

Zona, D., Gioli, B., Commane, R., Lindaas, J., Wofsy, S. C., Miller, C. E., Dinardo, S. J., Dengel, S., Sweeney, C., Karion, A., Chang, R. Y.-W., Henderson, J. M., Murphy, P. C., Goodrich, J. P., Moreaux, V., Liljedahl, A., Watts, J. D., Kimball, J. S., Lipson, D. A., and Oechel, W. C.: Cold season emissions dominate the Arctic tundra methane budget, P. Natl. Acad. Sci. USA, 113, 40–45, 2016.